Materials Today Bio 32 (2025) 101725

Contents lists available at ScienceDirect

Materials Today Bio

journal homepage: www.journals.elsevier.com/materials-today-bio

pH-responsive nanovesicles capable of remodeling the tumor microenvironment enable activatable near-infrared-II fluorescence image-guided enhanced radiotherapy

Lin Zhao [a,b,1], Mengzhen Wang [b,1], Yang Sun [a], Jinpeng Xu [a], Qinrui Fu [b,**], Wenjing Xiao [a,*]

[a] Department of Radiotherapy, The Affiliated Hospital of Qingdao University, Qingdao University, Qingdao, 266021, China
[b] Institute of Chronic Disease, College of Medicine, Qingdao University, Qingdao, 266021, China

ARTICLE INFO

Keywords:
Radiotherapy
Nanodrug
pH responsive
Near-infrared-II fluorescence imaging
Radiosensitization
Cancer

ABSTRACT

Traditional radiotherapy (RT) lacks the precision to distinguish between tumor and normal tissues, leading to inevitable X-ray-induced side effects in patients. Therefore, it is crucial to develop integrated imaging and therapeutic modalities that can reduce side effects on surrounding healthy tissues while enhancing susceptibility to tumor tissues. In this study, we developed a pH-responsive nanodrug (AuNRs-Mn_3O_4-Ag_2S Ve) by self-assembling the second near-infrared (NIR-II, 950–1700 nm) fluorescent probe Ag_2S quantum dots (QDs), multifunctional nanozyme Mn_3O_4 nanoparticles (NPs), and radiosensitizer gold nanorods (AuNRs) into a single nanoplatform *via* an emulsion process. This nanodrug enables precise tumor localization for accurately guided RT and multi-angle sensitization of RT. Upon intravenous administration, the nanodrug disintegrates in the tumor area due to the pH-sensitive polymer P4VP, releasing Ag_2S QDs which are specifically activated by the acidic environment, thereby "turning on" the NIR-II fluorescence signal. The optimal timing of the NIR-II fluorescence signal within the tumor region after intravenous injection was investigated, providing a reference for guided RT. *In vitro* and *in vivo* experiments confirmed the efficient enhancement of tumor radiosensitization by AuNRs and Mn_3O_4 NPs. The specific imaging modality that transitions the fluorescence signal from "off" to "on" has been successfully implemented, addressing the limitations of conventional RT and enhancing radiosensitivity. The integration of imaging and therapeutic approaches in this study presents a promising modality for image-guided tumor RT.

1. Introduction

As a leading cause of human health threats, malignant tumors continue to pose a significant risk to patients' lifespan [1,2]. According to the latest statistics from the World Health Organization (WHO) [3,4], RT remains one of the primary modalities for cancer treatment, having contributed to the cure of over 50 % of cancer patients [5]. The mechanism of RT can be broadly categorized into two pathways: direct damage to DNA double-strands by high-energy irradiation and indirect induction of necrosis or apoptosis in tumor cells through reactive oxygen species (ROS) generated by interactions with water molecules in the body [6], leading to DNA double-strand breaks and disrupting normal physiological processes in tumor cells. Common radiation types used in RT include photons (X-rays and γ-rays), electrons, protons, and neutrons, which are sourced from radioisotopes and radiation-producing devices. Among these modalities, X-ray-based RT is indispensable in clinical practice for treating locally advanced cancers and improving patient outcomes [7].

Nevertheless, X-ray induced RT inevitably has side effects that hinder its effectiveness. Firstly, traditional RT often causes unavoidable damage to surrounding healthy tissues due to the proximity of tumors to these tissues. Consequently, there is a need to develop ideal nano-radiosensitizers to enhance susceptibility to X-ray-induced lethality while minimizing side effects on normal tissues [8–10]. High-Z metal

This article is part of a special issue entitled: ECR board published in Materials Today Bio.

* Corresponding author.
** Corresponding author.
E-mail addresses: fuqinrui2022@qdu.edu.cn (Q. Fu), wjxiaomed@163.com (W. Xiao).

[1] LZ and MW contributed equally to this work.

https://doi.org/10.1016/j.mtbio.2025.101725
Received 12 February 2025; Received in revised form 25 March 2025; Accepted 1 April 2025
Available online 6 April 2025

nanomaterials have garnered significant attention as promising nano-radiosensitizers because of their strong X-ray attenuation coefficients and facile surface functionalization. Among these materials, gold nanorods (AuNRs) are particularly noteworthy for their excellent biocompatibility and ability to increase the radiosensitivity of tumor cells [11]. Secondly, radioresistance constitutes a significant cause of clinical RT failure and cancer progression, impeding the efficacy of RT [12]. The development of radioresistance is associated with multiple factors, including alterations in the tumor microenvironment (TME), cell cycle arrest, modifications in relevant genes, regulation of autophagy, and the presence of cancer stem cells. Among these factors, TME characteristics such as hypoxia and elevated glutathione (GSH) levels play a predominant role in promoting tumor recurrence and reducing treatment efficacy [13]. For instance, in many locally advanced solid tumors, the rapid proliferation of tumor cells outpaces angiogenesis, leading to abnormal blood vessel formation and structural disorder within tumor tissues, thereby failing to supply adequate oxygen [14]. Studies have shown that when oxygen levels are sufficiently high, tumor cell sensitivity to X-rays increases more than threefold [15]. Additionally, GSH levels significantly influence radiosensitivity under hypoxic conditions. Specifically, GSH is a rich endogenous antioxidant that maintains cellular redox homeostasis and mitigates ROS-induced cell damage [16]. Post-radiotherapy, increased ROS production can induce oxidative stress and DNA damage in cancer cells, highlighting the critical role of GSH in combating oxidative stress. Fortunately, discovery of manganese oxide nanomaterials, such as Mn_3O_4 NPs, has led to significant advancements. These materials can reverse radioresistance by responding to the TME and mimicking the natural enzymatic activities of glutathione peroxidase (GPX) and catalase under acidic tumor conditions [17]. Specifically, these NPs can convert GSH to its oxidized form (GSSH) under acidic conditions and catalyzing the decomposition of overexpressed hydrogen peroxide (H_2O_2) into oxygen (O_2). This process alleviates tumor hypoxia, thereby enhancing the sensitivity of tumors to X-ray irradiation [18,19].

The precise localization of tumors and the selection of optimal RT initiation times are critical for enhancing tumor therapy efficacy. Fluorescence (FL) imaging in the second near-infrared window (NIR-II, 1000–1700 nm), particularly TME-responsive activatable imaging, offers a promising approach to achieve this goal. Ag_2S quantum dots (QDs) have emerged as a powerful NIR-II FL imaging probe [20], widely utilized in various applications such as imaging-guided tumor therapy, subcutaneous and transcranial thermometry, early tumor diagnosis, and dynamic monitoring of the cardiovascular system [21]. However, the continuous "ON" state of the NIR-II FL signal from Ag_2S QDs limits their disease specificity and ability to distinguish tumor tissues from normal tissues, thereby constraining their broader application [22]. Fortunately, recent studies have shown that Ag_2S QDs assemblies can quench the NIR-II fluorescence signal, which is subsequently reactivated upon disintegration in response to the TME. This activation mechanism enables accurate tumor localization and guides the appropriate timing for therapeutic intervention.

Normal tissues typically exhibit a pH range of 7.0–7.5, whereas the TME has a significantly lower pH value of approximately 5.4 [23]. Leveraging this distinct characteristic, we developed a pH-responsive multifunctional hybrid nanovesicle (Ve), designated as AuNRs-M-n_3O_4-Ag_2S Ve, for NIR-II fluorescence (FL) imaging-guided precise RT (Fig. 1). The AuNRs-Mn_3O_4-Ag_2S Ve was fabricated through self-assembly *via* an emulsion process, incorporating gold nanorods (AuNRs), NIR-II fluorescent probes (Ag_2S QDs), and manganese oxide nanoparticles (Mn_3O_4 NPs) coated with a mixed polyethylene glycol-thiol (PEG-SH) and pH-sensitive polystyrene-co-4-vinylpyridine (HS-PS-P4VP) polymer. In these vesicular nanostructures, AuNRs absorb strong photons at 808 nm *via* robust plasmonic coupling, competing with Ag_2S QDs as an excitation source, resulting in fluorescence quenching. Upon reaching the tumor region, the AuNRs-Mn_3O_4-Ag_2S Ve dissociates to release Ag_2S QDs, thereby activating the NIR-II FL signal to guide RT. Additionally, AuNRs serve as radiosensitizers, while Mn_3O_4 regulates the TME by alleviating hypoxia and reducing glutathione (GSH), thus enhancing the generation of reactive oxygen species (ROS) to improve RT efficacy upon X-ray irradiation. This study exemplifies the advancement of precision medicine by facilitating activatable image-guided sensitization RT *via* the modulation of the TEM using nanozyme.

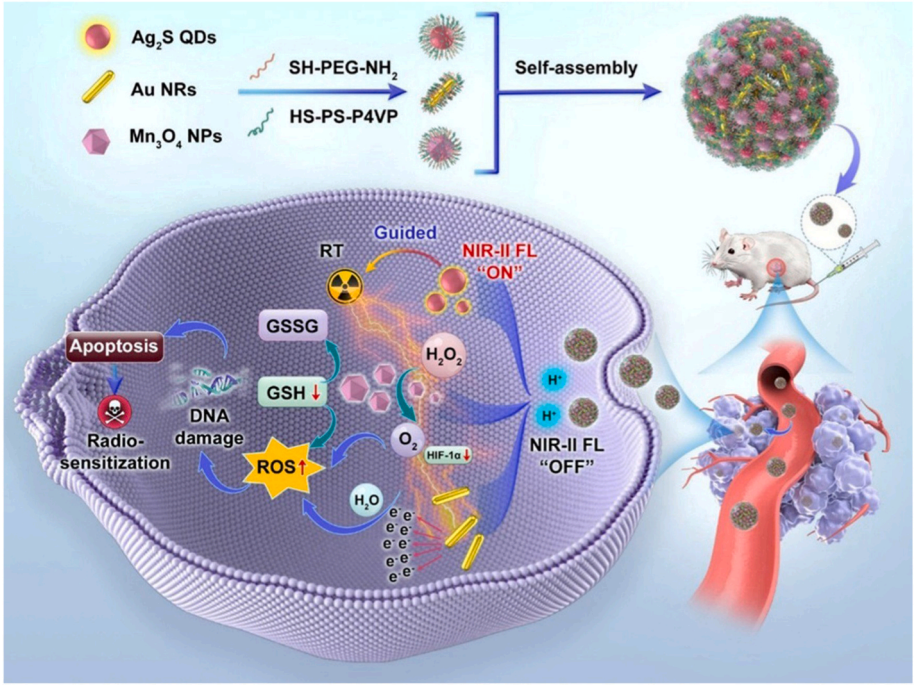

Fig. 1. Schematic illustration of the preparation process of AuNRs-Mn_3O_4-Ag_2S Ve and their application in activatable NIR-II fluorescence imaging-guided RT.

2. Results and discussion

2.1. Synthesis and characterization of AuNRs-Mn_3O_4-Ag_2S Ve

The AuNRs-Mn_3O_4-Ag_2S Ve was synthesized *via* the self-assembly of amphiphilic polymer-functionalized AuNRs, Mn_3O_4 NPs, and Ag_2S QDs. The mean diameter of the AuNRs was 35 nm, synthesized using a modified seedless growth method as previously reported (Fig. 2A) [24–26]. Concurrently, the ≈8 nm Ag_2S QDs were prepared through an evolutionary thermal decomposition process (Fig. 2B). Similarly, the ≈4 nm Mn_3O_4 NPs were synthesized *via* a modified solvothermal approach (Fig. 2C). Subsequently, pH-responsive thiolated polystyrene-co-poly (4-vinylpyridine) (HS-PS-P4VP) and hydrophilic poly(ethylene glycol)-thiol (SH-PEG-NH_2) polymers were covalently conjugated to the surfaces of the pre-prepared AuNRs, Mn_3O_4 NPs, and Ag_2S QDs *via* stable metal-sulfur bonds. Given that HS-PS-P4VP and SH-PEG-NH_2 possess positive charges, their conjugation to AuNRs, Mn_3O_4 NPs, or Ag_2S QDs resulted in an increase in zeta potential (Fig. S1), which confirms the successful attachment of these polymers to the nanomaterial surfaces. Finally, the multifunctional hybrid AuNRs-Mn_3O_4-Ag_2S Ve was successfully assembled using an oil-in-water emulsion method, with the molar ratio of AuNRs, Mn_3O_4 NPs, and Ag_2S QDs being 6:2:9 (Fig. S2). Moreover, based on the X-ray diffraction (XRD) pattern, the excellent crystalline structures of AuNRs, Mn_3O_4 NPs, Ag_2S QDs, and AuNRs-Mn_3O_4-Ag_2S Ve were also characterized to demonstrate the superior crystal properties of these nanomaterials. (Fig. S3). The representative transmission electron microscopy (TEM) images of AuNRs-Mn_3O_4-Ag_2S Ve clearly displayed spherical nanovesicles with excellent uniformity and dispersity (Fig. 2D). Higher magnification TEM images revealed that Ag_2S QDs and Mn_3O_4 NPs were densely packed around the AuNRs core (Fig. S4). Additionally, dynamic light scattering (DLS) analysis confirmed the successful self-assembly of the three components, with the resulting AuNRs-Mn_3O_4-Ag_2S Ve measuring approximately 200 nm in diameter (Fig. S5). Elemental mapping further corroborated the presence of Au, Ag, S, and Mn elements, providing definitive evidence of the composition of the AuNRs-Mn_3O_4-Ag_2S Ve (Fig. 2E).

In addition, X-ray photoelectron spectroscopy (XPS) was employed to analyze the chemical composition and valence states of Mn 2p, Mn 3s, and O 1s in the Mn_3O_4 NPs of the AuNRs-Mn_3O_4-Ag_2S Ve. This analysis provided precise insights into the electronic structure of Mn_3O_4 within the AuNRs-Mn_3O_4-Ag_2S Ve system. Previous studies have reported that the bimodal binding energy differences for Mn^{2+} and Mn^{3+} in Mn 3s are 5.9 eV and 5.5 eV, respectively. As illustrated in Fig. 2F, the observed bimodal binding energy difference of 5.7 eV for Mn 3s suggests the coexistence of Mn^{2+} and Mn^{3+} valence states in the Mn_3O_4 component of AuNRs-Mn_3O_4-Ag_2S Ve. Notably, the as-prepared AuNRs-Mn_3O_4-Ag_2S Ve demonstrated exceptional water solubility and stability owing to the high-density PEG polymer modification. When incubated with phosphate-buffered saline (PBS), cell culture medium, or cell culture medium supplemented with fetal bovine serum (FBS) for 7 days, no significant aggregation or precipitation was observed (Fig. S6), and the diameters remained unchanged across different media (Fig. S7). As a comparison, we synthesized the non-responsive AuNRs-Mn_3O_4-Ag_2S Ve through the analogous method after replacing the HS-PS-P4VP with HS-PS, whose diameters was also almost 200 nm (Fig. S8).

2.2. pH-responsive properties of AuNRs-Mn_3O_4-Ag_2S Ve

The pH difference between the TME and normal tissue offers a viable opportunity for developing specifically activated nanodrugs, which in turn facilitates subsequent NIR-II fluorescence imaging to guide tumor RT. Consequently, we investigated the specific activation properties of

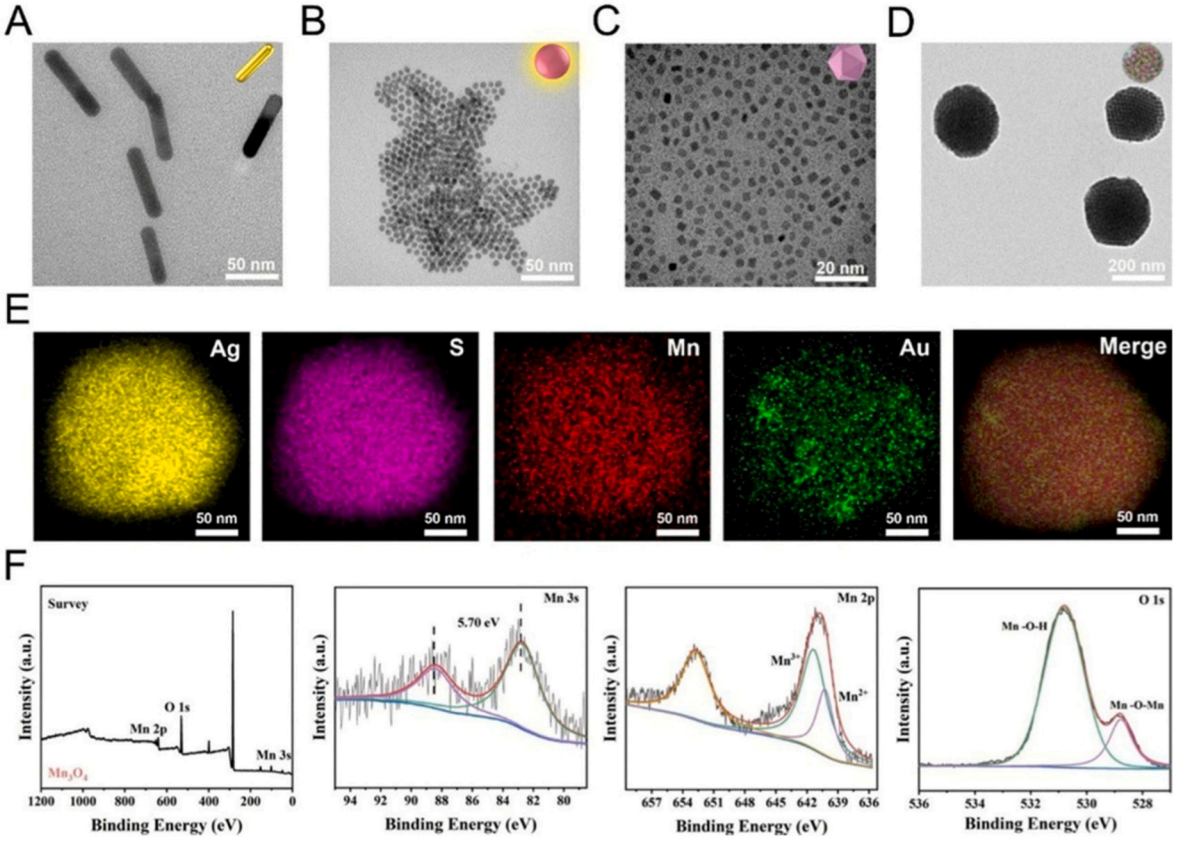

Fig. 2. Characterization of AuNRs-Mn_3O_4-Ag_2S Ve. Transmission electron microscopy (TEM) of (A) AuNRs, (B) Ag_2S QDs, (C) Mn_3O_4 NPs, (D) AuNRs-Mn_3O_4-Ag_2S Ve. (E) The corresponding elemental mapping demonstrates the distribution of Ag, S, Mn, and Au. (F) XPS analysis of Mn 3s, Mn 2p and O 1s spectra of Mn_3O_4 NPs.

AuNRs-Mn_3O_4-Ag_2S Ve transitioning from an "OFF" to an "ON" state in response to an acidic environment (Fig. 3A). Prior to this, we examined the pH responsiveness of the AuNRs-Mn_3O_4-Ag_2S Ve. After incubation in a pH 5.4 solution for 2 h, the vesicles gradually disassembled into individual AuNRs, Mn_3O_4, and Ag_2S. DLS data indicated a reduction in the size of the hybrid vesicles during the disassembly process under acidic conditions (Fig. 3B). More intuitively, representative TEM images illustrated the disassembly process of the AuNRs-Mn_3O_4-Ag_2S Ve (Fig. 3C). This disassembly is attributed to the pH-responsive characteristic of the HS-PS-P4VP polymer, where pyridine groups rapidly protonate under acidic conditions, leading to the breakdown of the nanovesicles. Subsequently, we observed a distinct enhancement in the NIR-II FL intensity of AuNRs-Mn_3O_4-Ag_2S Ve treated with acidic solution over time (Fig. 3D). This phenomenon can be attributed to the strong photon absorption of AuNRs within the vesicles (Fig. S9), which competes with the excitation light and subsequently suppresses the NIR-II FL signals from Ag_2S QDs [27–29]. However, under acidic conditions, the AuNRs-Mn_3O_4-Ag_2S Ve disassemble, leading to the release of Ag_2S QDs and the restoration of the NIR-II FL signal excited at 808 nm. Consequently, the NIR-II FL imaging of AuNRs-Mn_3O_4-Ag_2S Ve also showed a significant increase when treated with PBS solution at pH 5.4 over a period of 2 h (Fig. 3E, Fig. S10). These results demonstrated the remarkable pH responsive "turn-on" properties of AuNRs-Mn_3O_4-Ag_2S Ve.

2.3. The enzyme-like properties of AuNRs-Mn_3O_4-Ag_2S Ve

The elevated GSH levels and hypoxic conditions within the TME significantly impair the efficiency of RT. Nanomedicine that can effectively reduce GSH levels and generate oxygen has the potential to enhance RT efficacy by remodeling the TME. Consequently, we assessed the GSH depletion capacity and oxygen generation capability of AuNRs-Mn_3O_4-Ag_2S Ve, which exhibits GPX and CAT nanozyme activities (Fig. 4A). The dissolved oxygen meter was utilized to assess the oxygen-producing capacity of AuNRs-Mn_3O_4-Ag_2S Ve. Initially, we incubated AuNRs-Mn_3O_4-Ag_2S Ve in an acidic solution for a specified duration. As anticipated, the dissociated Mn_3O_4 NPs reacted with H_2O_2 to generate increased levels of oxygen due to their catalase-like enzymatic activity (Fig. 4B). In contrast, the control group of AuNRs-Ag_2S Ve exhibited negligible oxygen production, indicating that the oxygen generation primarily originates from the Mn_3O_4 NPs. Digital photographs provided a more intuitive visualization of bubble formation in the experimental group, thereby the oxygen production capacity of AuNRs-Mn_3O_4-Ag_2S Ve was further demonstrated (Fig. 4C). We subsequently utilized UV–visible spectroscopy with 5,5′-dithiobis-(2-nitrobenzoic acid) (DTNB) as a probe to evaluate the GSH depletion capability of Mn_3O_4 NPs derived from the disaggregated AuNRs-Mn_3O_4-Ag_2S Ve in an acidic solution. The presence of GSH leads to the transformation of DTNB into a yellow thiols-containing product, TNB, which exhibits characteristic absorbance at 412 nm. A significant reduction in the absorbance of DTNB at 412 nm was observed with increasing concentrations of AuNRs-Mn_3O_4-Ag_2S Ve in the acidic solution, indicating effective GSH depletion

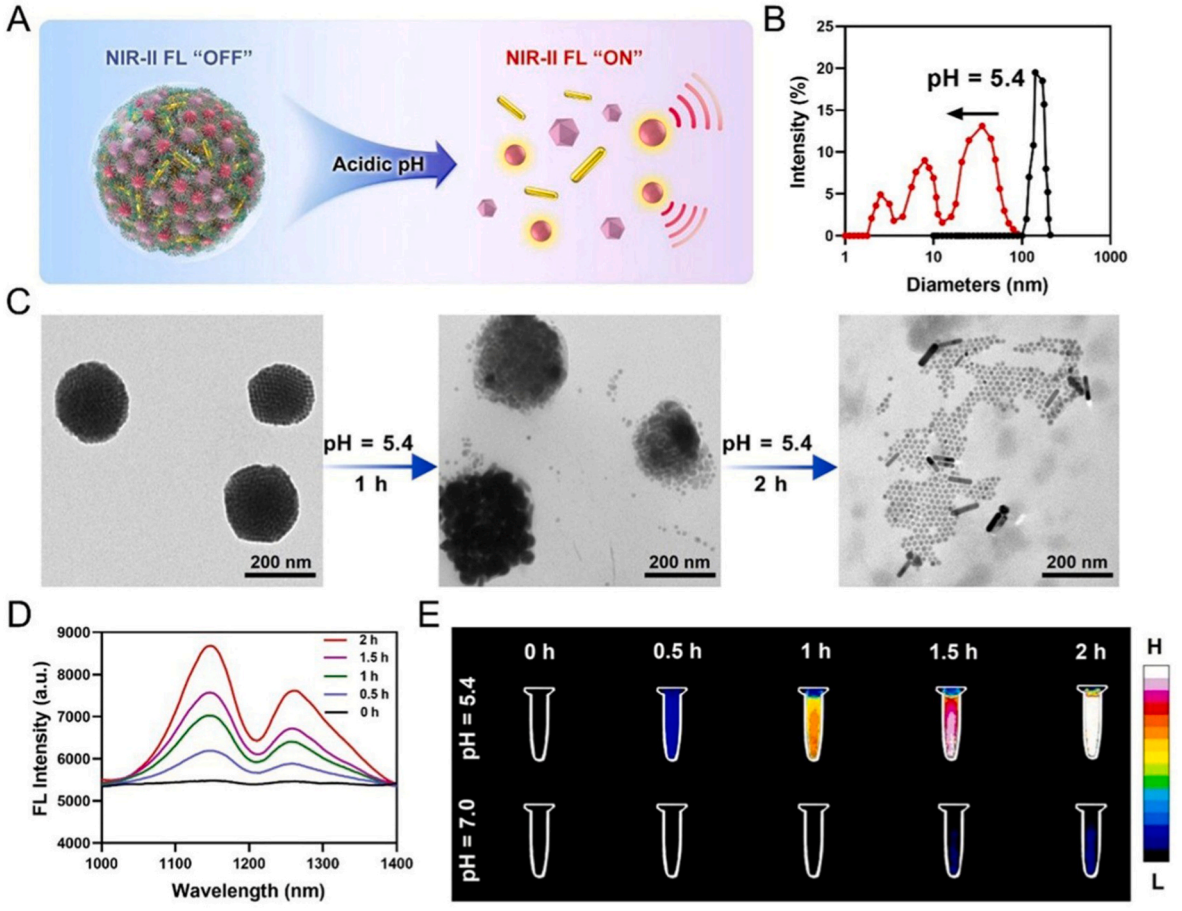

Fig. 3. pH responsive properties of AuNRs-Mn_3O_4-Ag_2S Ve (A) Schematic illustration of the pH-triggered NIR-II fluorescence signal activation by AuNRs-Mn_3O_4-Ag_2S Ve. (B) Hydrodynamic diameter changes and (C) TEM images of the pH-responsive AuNRs-Mn_3O_4-Ag_2S Ve before and after incubation in an acidic solution (pH = 5.4). (D) The variation in NIR-II FL spectra of AuNRs-Mn_3O_4-Ag_2S Ve incubated in an acidic solution over a 2 h period. (E) NIR-II FL images (Ex: 808 nm, Em: 1250 nm) of AuNRs-Mn_3O_4-Ag_2S Ve after incubation with solutions of varying pH values over a 2 h period.

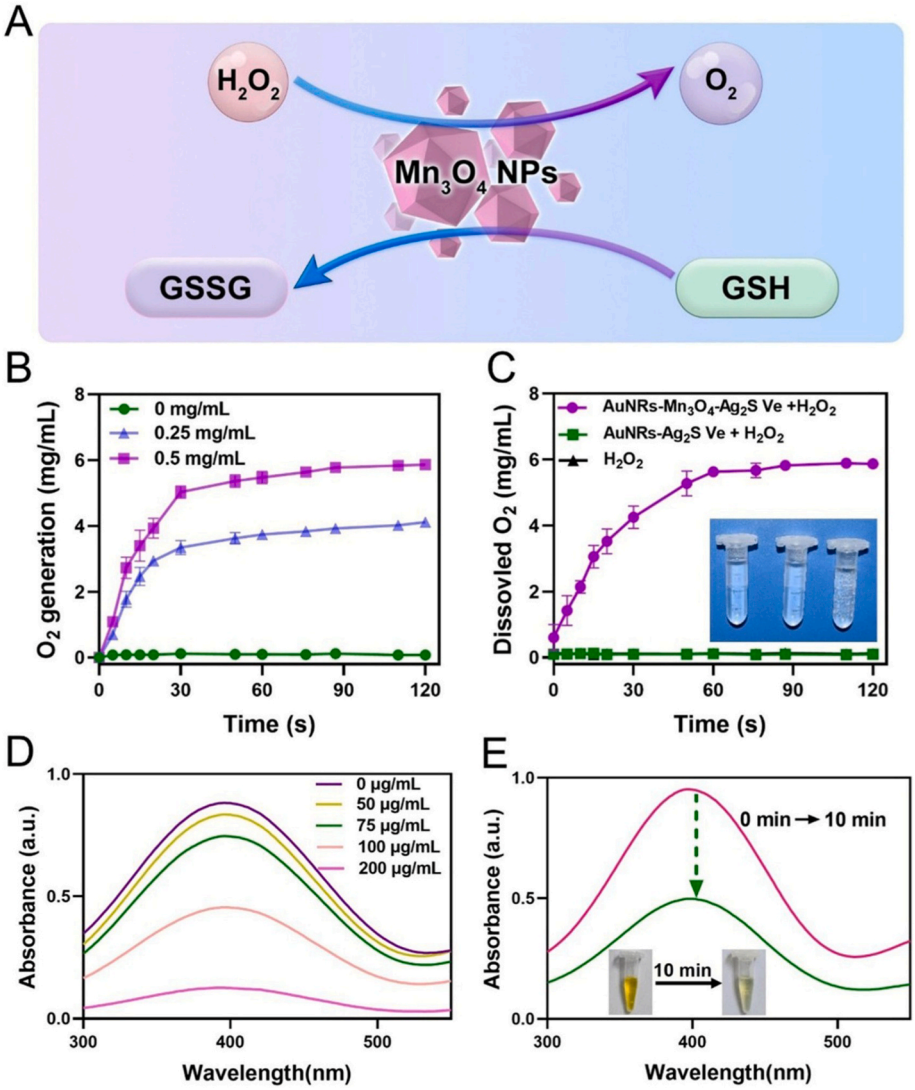

Fig. 4. The enzyme-like properties of AuNRs-Mn_3O_4-Ag_2S Ve (A) Schematic representation of the enzyme-like activities exhibited by Mn_3O_4 NPs dissociated from the AuNRs-Mn_3O_4-Ag_2S Ve in an acidic environment. (B) The O_2 production from various concentrations of AuNRs-Mn_3O_4-Ag_2S Ve in acidic solution upon addition of H_2O_2. (C) The O_2 generation capacity and corresponding digital images of different groups following 120 s of incubation with H_2O_2. (D) Concentration-dependent absorbance changes in GSH consumption following treatment with AuNRs-Mn_3O_4-Ag_2S Ve. (E) Time-dependent absorbance changes of GSH consumption upon treatment with AuNRs-Mn_3O_4-Ag_2S Ve.

by the Mn_3O_4 NPs (Fig. 4D). Additionally, the characteristic UV–vis absorption peak at 412 nm decreased over time (Fig. 4E), and visual color changes further confirmed GSH consumption. These characteristics indicated that AuNRs-Mn_3O_4-Ag_2S Ve has the potential to enhance RT sensitivity by decreasing intratumoral GSH overexpression and mitigating tumor hypoxia.

2.4. Biocompatibility and radiotherapeutic efficacy of AuNRs-Mn_3O_4-Ag_2S Ve in vitro

Exceptional biocompatibility is a prerequisite for the further biomedical application of nanodrugs. Therefore, we selected the 4T1 mouse mammary carcinoma cell line to evaluate the biocompatibility of AuNRs-Mn_3O_4-Ag_2S Ve *in vitro*. Initially, we examined the cellular uptake efficiency of DIL-labeled AuNRs-Mn_3O_4-Ag_2S Ve in 4T1 cells. Confocal laser scanning microscopy (CLSM) images clearly demonstrated that DIL-labeled AuNRs-Mn_3O_4-Ag_2S Ve gradually accumulated within the cytoplasm over time, indicating efficient cellular internalization and suggesting excellent biocompatibility (Fig. 5A). Additionally, the cytotoxicity of both responsive and non-responsive AuNRs-Mn_3O_4-Ag_2S Ve to 4T1 tumor cells and normal human kidney-2 (HK-2) cells was assessed using the CCK8 assay. The results showed that cell viability remained approximately 90 % even at a high concentration of 200 μg/mL, further confirming the superior biocompatibility of AuNRs-Mn_3O_4-Ag_2S Ve (Fig. 5B, Fig. S11).

Upon entering the tumor cells, AuNRs-Mn_3O_4-Ag_2S Ve could disassemble into three well-dispersed NPs under the acidic TME. Specifically, Mn_3O_4 NPs could catalyze oxidase-like enzymatic reactions to promote O_2 generation, thereby alleviating hypoxia and consequently enhancing ROS accumulation to increase radiosensitivity. Moreover, to further investigate the underlying mechanism of elevated O_2 levels mediated by Mn_3O_4 NPs, we conducted Western blotting analysis of hypoxia-inducible factor-1 alpha (HIF-1α) protein expression. As shown in Fig. S12, the results demonstrated a significant reduction in HIF-1α expression in the AuNRs-Mn_3O_4-Ag_2S Ve-treated group compared to the control groups. Therefore, the Mn_3O_4 NPs in AuNRs-Mn_3O_4-Ag_2S Ve exhibited promising catalase-like activity for relieving hypoxia. Besides, we utilized the tris(4,7-diphenyl-1,10-phenanthroline)ruthenium(II) dichloride (RDPP) as an oxygen fluorescent probe to detect O_2 production ability. RDPP is a porphyrin complex featuring a long fluorescence

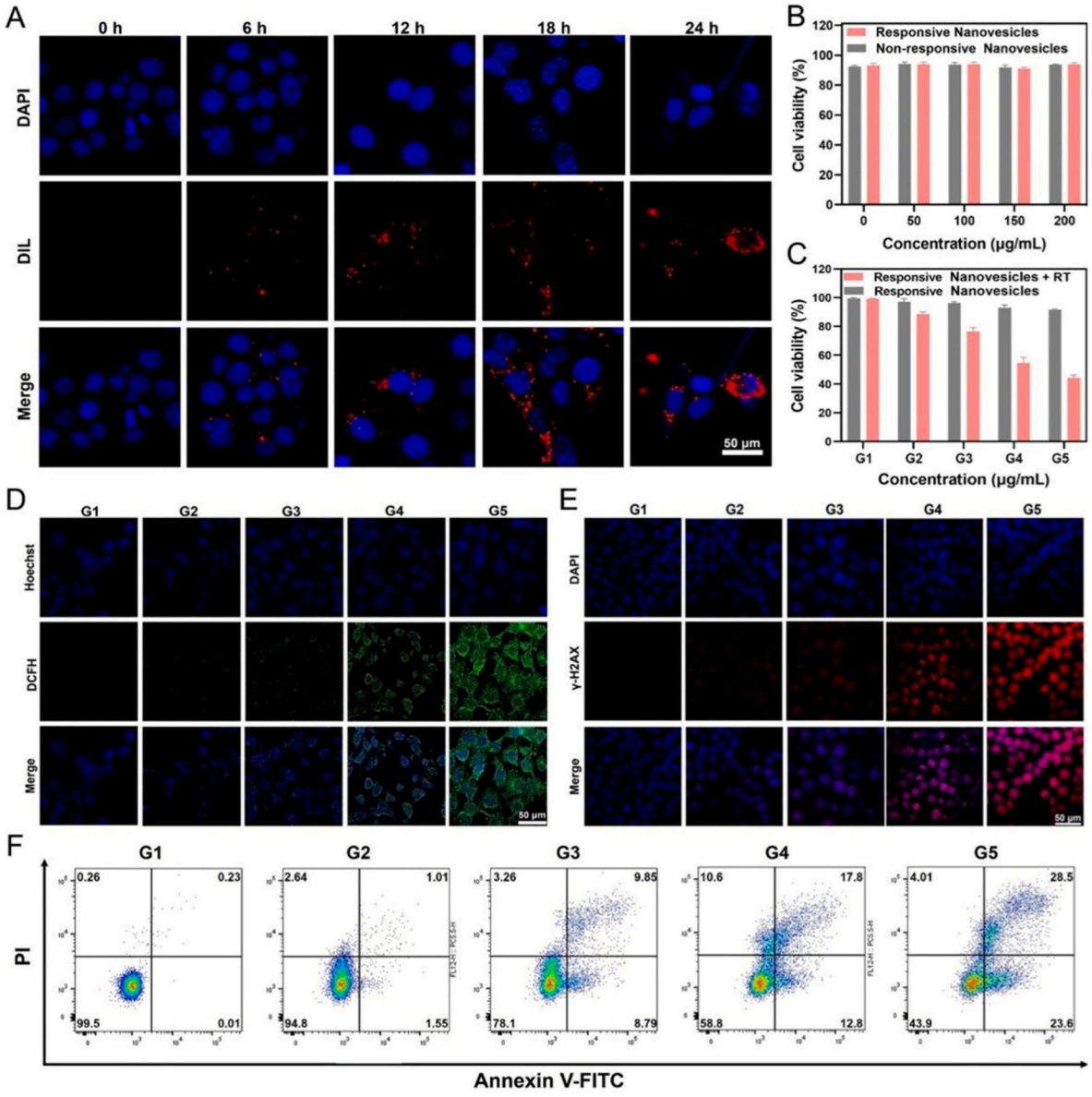

Fig. 5. *In vitro* radiosensitizing efficacy of AuNRs-Mn_3O_4-Ag_2S Ve. (A) Representative confocal fluorescence images of 4T1 cells incubated with DIL-labeled pH-responsive AuNRs-Mn_3O_4-Ag_2S Ve at various time points; scale bar: 50 μm. (B) The cell viability of 4T1 cells was assessed after incubation with varying concentrations of NPs. (C) Evaluation of the viability of 4T1 cells following various treatments. (D) Fluorescence images of intracellular ROS stained by DCFH-DA under different treatment conditions; scale bar = 50 μm. (E) Confocal fluorescence microscope images of 4T1 cells stained with γ-H2AX (indicating DNA damage) and DAPI (nuclear staining) following various treatments; scale bar: 50 μm. (F) Flow cytometry analysis was conducted on 4T1 cells following various treatments. (G1: PBS, G2: AuNRs-Mn_3O_4-Ag_2S Ve only, G3: X-ray only, G4: AuNRs-Ag_2S QDs Ve + X-ray, G5: AuNRs-Mn_3O_4-Ag_2S Ve + X-ray).

lifetime and high sensitivity to O_2 [30]. Oxygen molecules, acting as an efficient fluorescence quencher, can interact with fluorescent probes such as RDPP, resulting in a decrease in fluorescence intensity or a shortening of fluorescence lifetime. In hypoxic environments, the fluorescence intensity of the probe is relatively high; as the oxygen concentration increases, the fluorescence intensity gradually decreases. By measuring the changes in fluorescence intensity, the oxygen concentration can be quantitatively detected. As shown in Fig. S13, the green fluorescence of 4T1 cell treated by the AuNRs-Mn_3O_4-Ag_2S Ve was the weakest, suggesting that AuNRs-Mn_3O_4-Ag_2S Ve-treated cell could generate more O_2.

Additionally, the intracellular GSH content after various treatments was measured using a GSH detection kit. In the AuNRs-Mn_3O_4-Ag_2S Ve group, the GSH content, as determined by a standard curve, was found to be the lowest. This result suggests that the Mn_3O_4 NPs in the AuNRs-Mn_3O_4-Ag_2S Ve formulation effectively depleted GSH, thereby further validating its GPX-like enzyme activity (Fig. S14). Consequently, the AuNRs-Mn_3O_4-Ag_2S Ve system can enhance the efficacy of RT by alleviating tumor hypoxia and depleting GSH.

Encouraged by the outstanding biocompatibility and radiosensitizing mechanism of AuNRs-Mn_3O_4-Ag_2S Ve, we further investigated its pH-responsive radiosensitizing effect for biomedical applications *in vitro*. The CCK8 assay demonstrated that cell viability significantly decreased after incubation with AuNRs-Mn_3O_4-Ag_2S Ve at a concentration of 100 μg/mL followed by X-ray irradiation (Fig. 5C). This phenomenon can be attributed to the excellent radiosensitizing properties of AuNRs as high-Z metal elements and the radiosensitizing capabilities of Mn_3O_4 NPs. Furthermore, ROS, which are key molecules produced during oxidative stress and naturally generated from various organelles through typical biochemical reactions [31], can induce DNA damage *via* their strong oxidizing power, thereby directly destroying tumor tissues. To detect ROS production, we used 2′,

7′-dichlorofluorescin diacetate (DCFH-DA), which rapidly oxidizes to produce the strongly green fluorescent signal product 2′,7′-dichlorofluorescein (DCF) to determine ROS levels. In the control groups, treatments with only AuNRs-Mn_3O_4-Ag_2S Ve or X-ray irradiation alone exhibited negligible fluorescent signals. Excitingly, the fluorescent images clearly showed that the green fluorescent signal was highest in the group treated with AuNRs-Mn_3O_4-Ag_2S Ve combined with X-ray irradiation (Fig. 5D). This result is likely due to the excessive ROS production from the radiosensitizing effect of AuNRs and the multifunctional nature of Mn_3O_4 NPs, which alleviate hypoxia and deplete GSH in an acidic environment.

Subsequently, γ-H2AX staining was employed to validate the presence of double-strand breaks (DSBs) in DNA within tumor cells, thereby assessing the efficacy of DNA damage induced by AuNRs-Mn_3O_4-Ag_2S Ve across various treatments (Fig. 5E). Minimal red fluorescence was observed in both the PBS group and the single AuNRs-Mn_3O_4-Ag_2S Ve group. Slight red fluorescent spots were detected within the cell nuclei exposed to 6 Gy RT alone. Notably, while the intensity of red fluorescence increased in the cell nuclei when AuNRs-Ag_2S Ve was exposed to 6 Gy irradiation, the brightest red fluorescence was observed in the AuNRs-Mn_3O_4-Ag_2S Ve + X-ray group. This indicated that the combination of AuNRs-Mn_3O_4-Ag_2S Ve with RT significantly intensified DSBs' damage. Furthermore, flow cytometry using an Annexin V-FITC/PI apoptosis detection kit corroborated this observation. The cell apoptosis rates varied significantly among different treatments. As anticipated, the highest apoptosis and necrosis rate of 56.1 % was recorded for the AuNRs-Mn_3O_4-Ag_2S Ve + X-ray irradiation group, which was markedly higher than the rates for the AuNRs-Mn_3O_4-Ag_2S Ve group alone (5.2 %), the RT group alone (21.9 %), and the AuNRs-Ag_2S Ve (without Mn_3O_4 NPs) + X-ray group (41.2 %) (Fig. 5F). All the aforementioned results collectively demonstrated the significant radiosensitizing effect and enhanced cell-killing capability of AuNRs-Mn_3O_4-Ag_2S Ve when combined with X-ray irradiation, thereby establishing a robust foundation for further *in vivo* biomedical research.

2.5. Acidic TEM-responsive NIR-II FL imaging-guided RT in vivo

We employed the aforementioned pH-responsive AuNRs-Mn_3O_4-Ag_2S Ve for further evaluation of its potential *in vivo* imaging-guided RT. The AuNRs-Mn_3O_4-Ag_2S Ve functions as an activatable probe that remains inactive until triggered by the overexpressed acidity within the TME. This feature addresses the "always on" fluorescence limitation of Ag_2S QDs, enabling a switch from "OFF" to "ON" in the acidic TME, thereby enhancing both imaging sensitivity and specificity.

Based on the activated FL signals observed in the NIR-II window [32, 33], we employed AuNRs-Mn_3O_4-Ag_2S Ve as imaging contrast agents in 4T1 tumor-bearing mice. The animal model was established by subcutaneously inoculating 4T1 tumor cells into BALB/c mice. All animal experiments were conducted in strict accordance with the guidelines for the care and use of laboratory animals and were approved by the Institutional Animal Care and Use Committee of Qingdao University. For *in vivo* NIR-II fluorescence imaging, AuNRs-Mn_3O_4-Ag_2S Ve was dispersed in PBS (200 μL, 2 mg/mL) and intravenously injected into 4T1 tumor-bearing mice *via* the tail vein. A clear temporal variation in NIR-II FL signal intensity was recorded over time (Fig. 6A). The pH-responsive AuNRs-Mn_3O_4-Ag_2S Ve group exhibited a detectable FL signal within the tumor region at 6 h post-injection, which peaked at 24 h and gradually diminished thereafter. In contrast, no significant changes in NIR-II FL signal were observed in the non-responsive AuNRs-Mn_3O_4-Ag_2S Ve group. The corresponding changes in average fluorescence intensity at 1250 nm within the tumor region were also monitored, which correlated well with the variations in NIR-II fluorescence signals observed in the tumor images (Fig. 6B). Furthermore, despite the liver, as a major metabolic organ, exhibiting only a slight signal, the FL signal intensity in

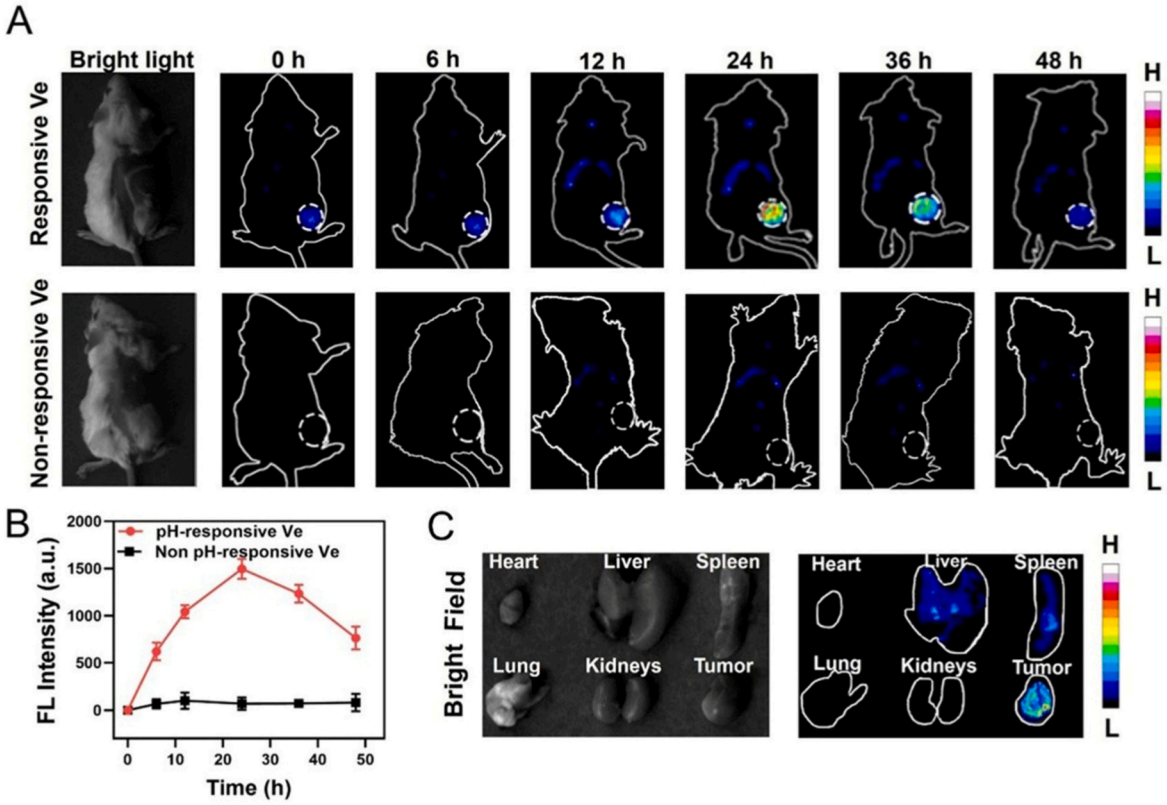

Fig. 6. *In vivo* NIR-II fluorescence imaging (Ex: 808 nm, Em: 1250 nm). (A) *In vivo* NIR-II fluorescence imaging of pH-responsive AuNRs-Mn_3O_4-Ag_2S Ve and non-responsive AuNRs-Mn_3O_4-Ag_2S Ve, as well as (B) the corresponding FL intensity. (C) *Ex vivo* fluorescence images of the dissected organs from the pH-responsive AuNRs-Mn_3O_4-Ag_2S Ve-treated group.

the tumor region was notably higher than that in the liver. The activation of the NIR-II fluorescence signal within the tumor can be attributed to the acid TME-induced dissociation of AuNRs-Mn_3O_4-Ag_2S Ve into Ag_2S QDs. The pH-responsive NIR-II fluorescence imaging was further confirmed by *ex vivo* imaging of major organs (Fig. 6C). These findings provided compelling evidence for the superior pH-responsive NIR-II FL imaging capabilities of AuNRs-Mn_3O_4-Ag_2S Ve, facilitating precise localization of tumor tissues and preparing for subsequent guided RT.

2.6. *In vivo* radiotherapeutic effect

Considering that the NIR-II FL signal peaked 24 h after intravenous injection [34–37], we selected this time point as optimal for irradiating and treating 4T1-tumor-bearing mice (Fig. 7A). The study included five groups of 4T1-tumor-bearing mice: Group 1 (G1) received PBS; Group 2 (G2) was treated with AuNRs-Mn_3O_4-Ag_2S Ve; Group 3 (G3) underwent X-ray irradiation alone; Group 4 (G4) was treated with AuNRs-Ag_2S QDs Ve followed by X-ray irradiation; and Group 5 (G5) received AuNRs-Mn_3O_4-Ag_2S followed by X-ray irradiation. Changes in tumor volume and body weight were visually captured using digital photos every 7 days post-treatment (Fig. 7B). Notably, tumors in G1 and G2 exhibited rapid growth despite treatment. In G3, while X-ray irradiation alone suppressed tumor growth to some extent, the inhibitory effect was not significant. This suggested that X-ray therapy without a radiosensitizer has limited therapeutic efficacy. In contrast, both G4 and G5 demonstrated excellent suppression of tumor growth compared to X-ray irradiation alone due to the use of a radiosensitizer. Particularly, G5, which received AuNRs-Mn_3O_4-Ag_2S Ve combined with X-ray irradiation, showed the most effective tumor inhibition among all X-ray-pretreated groups (Fig. 7C and D). Subsequently, we collected tumor tissues from each group of mice for morphological analysis using hematoxylin and eosin (H&E) staining after a 21-day treatment regimen (Fig. 7E).

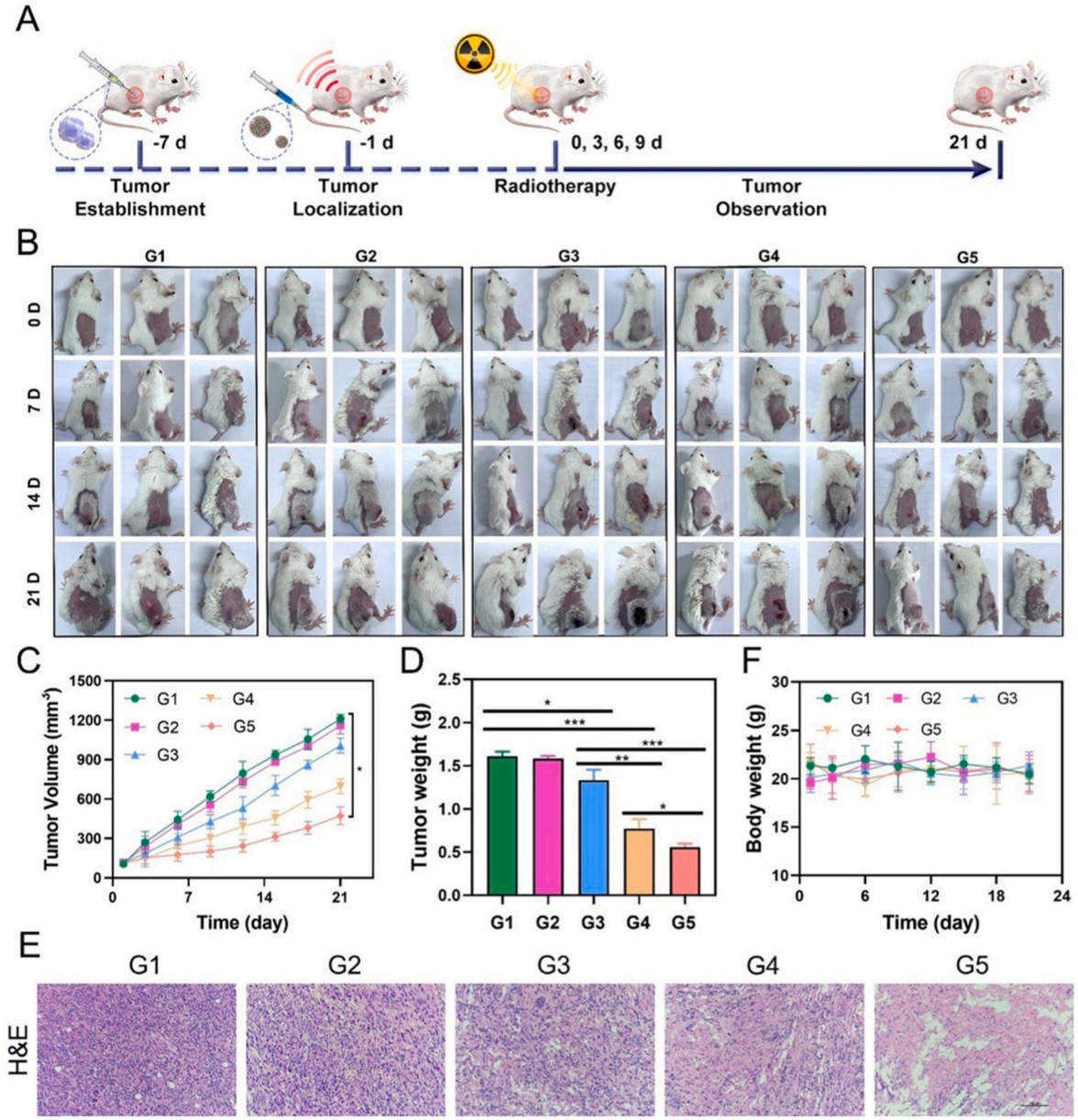

Fig. 7. *In vivo* radiosensitizing treatment. (A) Schematic illustration of the antitumor efficacy of AuNRs-Mn_3O_4-Ag_2S Ve in a 4T1 tumor-bearing mouse model. (B) Representative images of tumor-bearing mice before and after various treatments. (C) Tumor volume (D) Tumor weight (E) Representative H&E staining of tumor tissues from tumor-bearing mice after various treatments. (F) Body weight growth curves of 4T1 tumor-bearing BALB/c mice following different treatments. (G1: PBS, G2: AuNRs-Mn_3O_4-Ag_2S Ve only, G3: X-ray only, G4: AuNRs-Ag_2S QDs Ve + X-ray, G5: AuNRs-Mn_3O_4-Ag_2S Ve + X-ray). $^*P < 0.05$, $^{**}P < 0.01$, $^{***}P < 0.001$.

Compared to other groups, the tumor area treated with AuNRs-Mn_3O_4-Ag_2S Ve + X-ray exhibited the most pronounced apoptosis and necrosis, with significant structural disruption. This observation further corroborated its potent radiosensitizing effect. This study demonstrated that AuNRs-Mn_3O_4-Ag_2S Ve in combination with X-ray irradiation significantly enhanced radiosensitization, attributed to the multifunctional properties of Mn_3O_4 NPs as nano-enzymes to remodel the TME.

Furthermore, the body weight curves of mice showed no statistically significant differences between the control group and the AuNRs-Mn_3O_4-Ag_2S Ve-treated group during the 21-day post-treatment period (Fig. 7F). Blood analysis performed 21 days after treatment revealed no significant alterations in routine hematological parameters (Fig. S15), suggesting that the combination of AuNRs-Mn_3O_4-Ag_2S Ve and X-ray irradiation did not induce systemic toxicity. The biodistribution study of AuNRs-Mn_3O_4-Ag_2S Ve demonstrated that PEG modification enhanced its accumulation in the tumor region, reaching 10.35 ± 0.18 %ID g^{-1} at 24 h post-injection ([Au] %ID g^{-1}). However, AuNRs-Mn_3O_4-Ag_2S Ve was rapidly cleared from other major organs, with minimal residual NPs observed after 10 days (Fig. S16). Additionally, H&E staining of tissue sections from the liver, heart, spleen, lungs, and kidneys exhibited no significant pathological changes following therapy (Fig. S17), further confirming the safety of AuNRs-Mn_3O_4-Ag_2S Ve as a therapeutic agent for precise RT.

3. Conclusion

In summary, we developed a multifunctional pH-responsive nanodrug for NIR-II FL imaging-guided RT. Upon activation by the acidic TME, the AuNRs-Mn_3O_4-Ag_2S Ve disassembles due to the acid-sensitive polymer P4VP, sequentially releasing AuNRs, Mn_3O_4 NPs, and Ag_2S QDs. The combination of AuNRs' radiosensitizing effect with the multifaceted properties of Mn_3O_4 NPs as nanozymes, particularly their ability to alleviate hypoxia and reduce GSH, significantly enhances radiosensitization efficiency. The process simultaneously restores the NIR-II FL imaging signal, thereby enabling precise tumor localization. Consequently, this pH-responsive nanomedicine, which integrates an activatable FL probe and a potent radiosensitizer, shows significant potential for future clinical applications in image-guided RT.

CRediT authorship contribution statement

Lin Zhao: Writing – original draft, Resources, Methodology, Data curation. **Mengzhen Wang:** Visualization, Validation, Software, Investigation, Formal analysis. **Yang Sun:** Visualization, Software, Methodology, Conceptualization. **Jinpeng Xu:** Resources, Formal analysis, Conceptualization. **Qinrui Fu:** Writing – review & editing, Visualization, Project administration, Funding acquisition, Conceptualization. **Wenjing Xiao:** Writing – review & editing, Visualization, Supervision, Project administration, Conceptualization.

Ethics approval and consent to participate

All animal experiments were approved in accordance with current guidelines for the care of laboratory animals and were approved by the appropriate committees of Qingdao University.

Consent for publication

All authors agree to publish this manuscript.

Availability of data and materials

No datasets were generated or analysed during the current study.

Declaration of competing interest

The authors declare that they have no known competing financial interests or personal relationships that could have appeared to influence the work reported in this paper.

Acknowledgements

This work was supported by the Taishan Scholar Youth Expert Program in Shandong Province (Grant Number: tsqnz20230608), grants from the Natural Science Foundation of Shandong Province (Grant Number: ZR2023QB045), Scientific Research of Distinguished Professor from Qingdao University, China (Grant Number: DC2200000953, RZ2300002607, RZ2400001462), and grants from Natural Science Foundation of Qingdao Municipality, Shandong Province, China (Grant Number: 23-2-1-30-zyyd-jch).

Appendix A. Supplementary data

Supplementary data to this article can be found online at https://doi.org/10.1016/j.mtbio.2025.101725.

Data availability

Data will be made available on request.

References

[1] B. Freddie, L. Mathieu, W. Elisabete, S. Isabelle, The ever-increasing importance of cancer as a leading cause of premature death worldwide, Cancer 127 (16) (2021), https://doi.org/10.1002/cncr.33587.
[2] Y. Pan, W. Tang, W. Fan, J. Zhang, X. Chen, Development of nanotechnology-mediated precision radiotherapy for anti-metastasis and radioprotection, Chem. Soc. Rev. 51 (23) (2022) 9759–9830, https://doi.org/10.1039/D1CS01145F.
[3] Y. Chen, G. Song, Z. Dong, X. Yi, Y. Chao, C. Liang, K. Yang, L. Cheng, Z. Liu, Drug-loaded mesoporous tantalum oxide nanoparticles for enhanced synergetic chemoradiotherapy with reduced systemic toxicity, Small 13 (8) (2017) 1602869, https://doi.org/10.1002/smll.201602869.
[4] H. Sung, J. Ferlay, R.L. Siegel, M. Laversanne, I. Soerjomataram, A. Jemal, F. Bray, Global cancer statistics 2020: GLOBOCAN estimates of incidence and mortality worldwide for 36 cancers in 185 countries, CA Cancer J. Clin. 71 (3) (2021) 209–249, https://doi.org/10.3322/caac.21660.
[5] J. Ferlay, I. Soerjomataram, R. Dikshit, S. Eser, C. Mathers, M. Rebelo, D.M. Parkin, D. Forman, F. Bray, Cancer incidence and mortality worldwide: Sources, methods and major patterns in GLOBOCAN 2012, Int. J. Cancer 136 (5) (2015) E359–E386, https://doi.org/10.1002/ijc.29210.
[6] L. Zhao, Y. Sun, Q. Fu, W. Xiao, Emerging nanoradiosensitizers and nanoradioprotectants for enhanced cancer theranostics, Chem. Eng. J. 501 (2024) 157554, https://doi.org/10.1016/j.cej.2024.157554.
[7] N. Lv, X. Zhang, S. Wang, Y. Wu, X. Ge, J. Song, Q. Ma, S. Gao, Stimuli-responsive hybrid vesicle for tumor dual-model NIR-II photoacoustic and fluorescence imaging and precise radiotherapy, Adv. Opt. Mater. 10 (17) (2022) 2200694, https://doi.org/10.1002/adom.202200694.
[8] G. Song, L. Cheng, Y. Chao, K. Yang, Z. Liu, Emerging nanotechnology and advanced materials for cancer radiation therapy, Adv. Mater. 29 (32) (2017) 1700996, https://doi.org/10.1002/adma.201700996.
[9] R.A. Chandra, F.K. Keane, F.E.M. Voncken, C.R. Thomas, Contemporary radiotherapy: present and future, Lancet 398 (10295) (2021) 171–184, https://doi.org/10.1016/S0140-6736(21)00233-6.
[10] W. Xiao, L. Zhao, Y. Sun, X. Yang, Q. Fu, Stimuli-responsive nanoradiosensitizers for enhanced cancer radiotherapy, Small Methods 8 (1) (2024) 2301131, https://doi.org/10.1002/smtd.202301131.
[11] T. Chen, L. Su, X. Ge, W. Zhang, Q. Li, X. Zhang, J. Ye, L. Lin, J. Song, H. Yang, Dual activated NIR-II fluorescence and photoacoustic imaging-guided cancer chemo-radiotherapy using hybrid plasmonic-fluorescent assemblies, Nano Res. 13 (12) (2020) 3268–3277, https://doi.org/10.1007/s12274-020-3000-9.
[12] D. Schaue, W.H. McBride, Opportunities and challenges of radiotherapy for treating cancer, Nat. Rev. Clin. Oncol. 12 (9) (2015) 527–540, https://doi.org/10.1038/nrclinonc.2015.120.
[13] Y. Xiong, C. Xiao, Z. Li, X. Yang, Engineering nanomedicine for glutathione depletion-augmented cancer therapy, Chem. Soc. Rev. 50 (10) (2021) 6013–6041, https://doi.org/10.1039/D0CS00718H.
[14] L. Hua, Z. Wang, L. Zhao, H. Mao, G. Wang, K. Zhang, X. Liu, D. Wu, Y. Zheng, J. Lu, R. Yu, H. Liu, Hypoxia-responsive lipid-poly-(hypoxic radiosensitized polyprodrug) nanoparticles for glioma chemo- and radiotherapy, Theranostics 8 (18) (2018) 5088–5105, https://doi.org/10.7150/thno.26225.

[15] S. Rey, L. Schito, M. Koritzinsky, B.G. Wouters, Molecular targeting of hypoxia in radiotherapy, Adv. Drug Deliv. Rev. 109 (2017) 45–62, https://doi.org/10.1016/j.addr.2016.10.002.
[16] X. Lin, R. Zhu, Z. Hong, X. Zhang, S. Chen, J. Song, H. Yang, GSH-responsive radiosensitizers with deep penetration ability for multimodal imaging-guided synergistic radio-chemodynamic cancer therapy, Adv. Funct. Mater. 31 (24) (2021) 2101278, https://doi.org/10.1002/adfm.202101278.
[17] G. Huang, J. Zang, L. He, H. Zhu, J. Huang, Z. Yuan, T. Chen, A. Xu, Bioactive nanoenzyme reverses oxidative damage and endoplasmic reticulum stress in neurons under ischemic stroke, ACS Nano 16 (1) (2021) 431–452, https://doi.org/10.1021/acsnano.1c07205.
[18] M.C. Biesinger, B.P. Payne, A.P. Grosvenor, L.W.M. Lau, A.R. Gerson, R.S.C. Smart, Resolving surface chemical states in XPS analysis of first row transition metals, oxides and hydroxides: Cr, Mn, Fe, Co and Ni, Appl. Surf. Sci. 257 (7) (2011) 2717–2730, https://doi.org/10.1016/j.apsusc.2010.10.051.
[19] S. Pan, G. Huang, Z. Sun, X. Chen, X. Xiang, W. Jiang, Y. Xu, T. Chen, X. Zhu, X-Ray-responsive zeolitic imidazolate framework-capped nanotherapeutics for cervical cancer-targeting radiosensitization, Adv. Funct. Mater. 33 (13) (2023) 2213364, https://doi.org/10.1002/adfm.202213364.
[20] Y. Zhang, Y. Liu, C. Li, X. Chen, Q. Wang, Controlled synthesis of Ag_2S Quantum Dots and experimental determination of the exciton bohr radius, J. Phys. Chem. C 118 (9) (2014) 4918–4923, https://doi.org/10.1021/jp501266d.
[21] Z. Yuan, X. Liu, J. Ling, G. Huang, J. Huang, X. Zhu, L. He, T. Chen, T. Chen, In situ-transition nanozyme triggered by tumor microenvironment boosts synergistic cancer radio-/chemotherapy through disrupting redox homeostasis, Biomaterials 287 (2022) 121620, https://doi.org/10.1016/j.biomaterials.2022.121620.
[22] X. Zhang, W. Wang, L. Su, X. Ge, J. Ye, C. Zhao, Y. He, H. Yang, J. Song, H. Duan, Plasmonic-fluorescent Janus Ag/Ag_2S nanoparticles for in situ H_2O_2-activated NIR-II fluorescence imaging, Nano Lett. 21 (6) (2021) 2625–2633, https://doi.org/10.1021/acs.nanolett.1c00197.
[23] J. Clara-Rahola, A. Moscoso, A. Belén Ruiz-Muelle, M. Laurenti, P. Formanek, J. M. Lopez-Romero, I. Fernández, J.F. Diaz, J. Rubio-Retama, A. Fery, R. Contreras-Cáceres, Au@p4VP core@shell pH-sensitive nanocomposites suitable for drug entrapment, J. Colloid Interface Sci. 514 (2018) 704–714, https://doi.org/10.1016/j.jcis.2017.12.072.
[24] T. Liu, L. Tong, N. Lv, X. Ge, Q. Fu, S. Gao, Q. Ma, J. Song, Two-stage size decrease and enhanced photoacoustic performance of stimuli-responsive polymer-gold nanorod assembly for increased tumor penetration, Adv. Funct. Mater. 29 (16) (2019) 1806429, https://doi.org/10.1002/adfm.201806429.
[25] H. Feng, Q. Fu, W. Du, R. Zhu, X. Ge, C. Wang, Q. Li, L. Su, H. Yang, J. Song, Quantitative assessment of copper(II) in wilson's disease based on photoacoustic imaging and ratiometric surface-enhanced Raman scattering, ACS Nano 15 (2) (2021) 3402–3414, https://doi.org/10.1021/acsnano.0c10407.
[26] M.-F. Tsai, S.-H.G. Chang, F.-Y. Cheng, V. Shanmugam, Y.-S. Cheng, C.-H. Su, C.-S. Yeh, Au nanorod design as light-absorber in the first and second biological near-infrared windows for in vivo photothermal therapy, ACS Nano 7 (6) (2013) 5330–5342, https://doi.org/10.1021/nn401187c.
[27] T. Liu, X. Zhang, D. Liu, B. Chen, X. Ge, S. Gao, J. Song, Self-Assembled Ag2S-QD Vesicles for in Situ Responsive NIR-II Fluorescence Imaging-Guided Photothermal Cancer Therapy, vol. 9, 2021 2100233, https://doi.org/10.1002/adom.202100233, 12.
[28] H. Yang, Z. Ma, Q. Wang, Shortwave-infrared silver chalcogenide quantum dots for optoelectronic devices, ACS Nano 18 (44) (2024) 30123–30131, https://doi.org/10.1021/acsnano.4c11787.
[29] C. Li, Q. Wang, Challenges and opportunities for intravital near-infrared fluorescence imaging technology in the second transparency window, ACS Nano 12 (10) (2018) 9654–9659, https://doi.org/10.1021/acsnano.8b07536.
[30] M. Liu, H. Zhang, Y. Bao, G. Li, R. Yan, X. Wu, Z. Wang, Y. Jin, Immunogenic cell death induction and oxygenation by multifunctional hollow silica/copper-doped carbon dots, ACS Appl. Mater. Interfaces 16 (15) (2024) 18534–18550, https://doi.org/10.1021/acsami.4c00853.
[31] Q. Fu, L. Yu, M. Zhang, S. Li, L. Liu, Engineering nanosystems for ROS-bridged cancer cascade therapy, Chem. Eng. J. 473 (2023) 145415, https://doi.org/10.1016/j.cej.2023.145415.
[32] D. Ji, Y. Lin, X. Guo, B. Ramasubramanian, R. Wang, N. Radacsi, R. Jose, X. Qin, S. Ramakrishna, Electrospinning of nanofibres, Nat. Rev. Methods Primers 4 (1) (2024) 1, https://doi.org/10.1038/s43586-023-00289-w.
[33] D. Gao, Z. Luo, Y. He, L. Yang, D. Hu, Y. Liang, H. Zheng, X. Liu, Z. Sheng, Low-dose NIR-II preclinical bioimaging using liposome-encapsulated cyanine dyes, Small 19 (17) (2023) 2206544, https://doi.org/10.1002/smll.202206544.
[34] D. Hu, M. Zha, H. Zheng, D. Gao, Z. Sheng, Recent advances in indocyanine green-based probes for second near-infrared fluorescence imaging and therapy, Research 8 (2025) 583, https://doi.org/10.34133/research.0583.
[35] X. Ge, L. Su, Z. Chen, K. Zhu, X. Zhang, Y. Wu, J. Song, A radio-pharmaceutical fluorescent probe for synergistic cancer radiotherapy and ratiometric imaging of tumor reactive oxygen species, Angew. Chem. Int. Ed. 62 (29) (2023) e202305744, https://doi.org/10.1002/anie.202305744.
[36] Z. Wu, H. Chen, H. Zhang, L. Ye, J. Ke, Y. Liu, P. Sun, M. Hong, Construction of tumor-cell nucleus targeting lanthanide nano-prodrugs with lutetium-177 labelling for high-efficient tumor fluorescence-localization and radionuclide therapy, Nano Today 55 (2024) 102214, https://doi.org/10.1016/j.nantod.2024.102214.
[37] Y. Jin, D. Li, X. Zheng, M. Gao, W. Wang, X. Zhang, W. Kang, C. Zhang, S. Wu, R. Dai, Z. Zheng, R. Zhang, A novel activatable nanoradiosensitizer for second near-infrared fluorescence imaging-guided safe-dose synergetic chemo-radiotherapy of rheumatoid arthritis, Adv. Sci. 11 (17) (2024) 2308905, https://doi.org/10.1002/advs.202308905.